INDERSCIENCE PUBLISHERS
Linking academia, business and industry through research

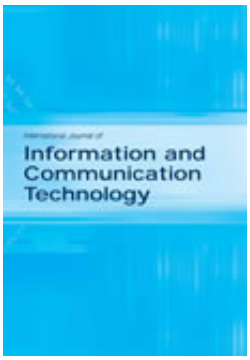

International Journal of Information and Communication Technology

ISSN online: 1741-8070 - ISSN print: 1466-6642
https://www.inderscience.com/ijict

Advancement in electromechanical systems for innovative product design

Yang Yang

DOI: 10.1504/IJICT.2025.10075082

Article History:

Received:	30 August 2025
Last revised:	11 September 2025
Accepted:	12 September 2025
Published online:	05 January 2026

Advancement in electromechanical systems for innovative product design

Yang Yang

Department of Basic,
Liaoning University of Science and Technology,
Benxi, Liaoning, 117004, China
Email: xiaomianqian66@163.com

Abstract: This paper presents advancements in electromechanical systems aimed at enhancing the precision and reliability of innovative product design through embedded sensing and intelligent control. A self-sensing electromechanical system is developed by integrating embedded time-grating displacement sensors into traditional mechanical structures, enabling high-resolution position detection of motors, worm gears, and bearings. Methods for current reconstruction using a single resistance sensor and error suppression through optimised light-field structures are proposed to improve detection accuracy. Experimental validation demonstrates significant improvements in measurement precision and error reduction through adaptive weighted data fusion. The findings highlight the potential of combining electromechanical design, sensing integration, and intelligent algorithms to support next-generation innovative product service systems (PSS).

Keywords: electromechanical systems; smart product service systems; embedded sensors; time-grating displacement; error correction; data fusion; MEMS actuators; condition monitoring.

Reference to this paper should be made as follows: Yang, Y. (2025) 'Advancement in electromechanical systems for innovative product design', *Int. J. Information and Communication Technology*, Vol. 26, No. 48, pp.60–79.

Biographical notes: Yang Yang is a researcher in the Department of Basic Studies at Liaoning University of Science and Technology, Benxi, China. His academic work focuses on applied mathematics, statistical modelling, and engineering-related analytical methods. He has contributed to several research projects involving data analysis, computational techniques, and interdisciplinary applications in science and technology. He is actively involved in teaching foundational courses and supporting undergraduate research. He continues to pursue research aimed at improving modelling accuracy and practical problem-solving in engineering and applied sciences.

1 Introduction

Research on the longevity of electrical machines has revealed that any part could break down; the likelihood of a failure depends on the kind, design, operating circumstances, and use of the equipment. Traditionally, the backbone of electrical equipment integrity monitoring has been offline diagnostics and thermal/vibration surveillance

(Terron-Santiago et al., 2021). Electrical monitoring instruments that avoid equipment and process failure while in operation have been the subject of extensive research due to the fact that they allow for inexpensive remote monitoring. Several reviews of the relevant literature highlight the investigation of electrical defect detection in relation to machine issues as the principal field of study. The shortcomings of electrical monitoring, such as false positives, have been shown by technology that has been utilised in the field for more than 20 years, low sensitivity, and difficulties in problem detection (Yea et al., 2020). Something else goes wrong with VFD operations when the number of converter motors increases. Therefore, in order to develop an open maintenance plan, recent research employs creative methods such as fault prognostics, intelligent algorithms, transient analysis, improved condition monitoring, air-gap and stray flux monitoring, and more. Traditional maintenance practices can be broadly classified into two groups: reactive and preventative (Akbar et al., 2023).

In contrast to preventative maintenance, which aims to thoroughly examine systems to determine if they require maintenance before a breakdown occurs, reactive maintenance is applied after the fact. Neither method is suitable for industrial usage, though, due to the enormous economic impact they would have. When a machine breaks down, reactive maintenance steps in to fix it, but this interrupts the process. Here, digitisation has a significant impact on the servitisation phenomenon. Manufacturing organisations have been adapting their business models to focus on supplying services alongside physical products to fulfil customer needs, thanks to servitisation, which has been going on for decades (Chen et al., 2021). While manufacturers had trouble organising themselves to deliver satisfactory services at first, digital technology may help them do so while also opening the door to new service possibilities. The term ‘data-driven offerings’ was coined as a result of the merging of physical goods and immaterial services with digital technology, specifically innovative PSS, as a result of the linking of digitalisation and servitisation, also known as digital servitisation (Langley et al., 2022). More and more, companies in the manufacturing sector are looking to expand their service offerings to include real-time product monitoring.

Services based on real-time product monitoring can be enabled with the help of internet of things (IoT) platforms, which are digital environments that connect people to products and other IoT devices. These platforms also include approaches for data analysis (Arioli et al., 2023). Maintenance, repair, and remanufacturing are services that help suppliers reduce their goods’ environmental impact, make their offerings more appealing, and boost customer happiness. Thanks to Moore’s law and its relentless advancement, the computing industry has been able to provide consumers worldwide with processing power that has grown exponentially over the past sixty years. Thanks to recent developments in lithography, materials science, and semiconductor technology, it is now possible to miniaturise electronics to the atomic level by packing billions of transistors onto a single chip (Spiliotis et al., 2020). These chips’ design processes have likewise seen significant evolution over the past few decades. All of the advancements in the industry, from manual design in the beginning to CAD and now to EDA tools helped by artificial intelligence (AI), would not have been possible without this shift in design techniques (Helmns et al., 2021). This means that they are a good fit for describing new concepts (Cirstea et al., 2024).

This article is organised in the following way: after a brief overview of previous research on electromechanical system developments in Section 2, the study’s

methodology for innovative product design is laid out. In Section 3, the results are provided, and in Section 4, the findings are presented. Lastly, Section 5 presents the study's conclusions.

1.1 Contribution of this study

This work primarily contributes by offering a unified framework for electromechanical systems that incorporates embedded displacement sensing, improved current reconstruction, and optical error suppression. The suggested method achieves great precision without using numerous sensors, which reduces complexity and costs compared to standard condition monitoring systems. Using data fusion across several components, the strategy greatly improves positioning accuracy and dependability. This research contributes to the design of self-sensing electromechanical systems and lays out a practical way for innovative product service systems (PSS) to be implemented in modern manufacturing settings. PSS will help with predictive maintenance, energy efficiency, and customer-oriented services.

2 Literature review

2.1 Electromechanical systems

In order to design and apply DTs across the aforementioned stages of the life cycle, it is crucial to have a virtual model that depicts the object's characteristics when they are functioning. Acceleration, braking, and shock/smooth load shift modes in rolling stand electromechanical systems are determined by the process, regardless of whether the rolls are made of metal or not (Abouzeid et al., 2022). Finding a happy medium between the mathematical complexity of Park-Gorev equations for variable frequency drives and the practicality of using simpler models that yet represent the operation's core is crucial when constructing DTs. When dealing with a particular issue, it is vital to remember this equilibrium (Fakhraian et al., 2023). As a result, keep in mind that the motor's 'external' coordinates should be the focus of simplified simulation models. These models need to accurately depict non-electrical characteristics, such as shaft torques, nonlinearities (such as gaps in mechanical joints), and the elastic properties of the kinematic gearbox (Gasiyarov et al., 2023). Research on rolling stand electromechanical systems often makes use of two-mass models; however, three-mass ones are not uncommon.

2.2 Smart PSS

Smart PSS, first presented by Valencia, is defined as meeting user needs through the integration of electronic services and intelligent products through the application of information and communication technology (ICT). Scholars generally agree with this reading; however, some have offered competing readings (Jalil et al., 2022). For instance, 'smart PSS' refers to a fully digitalised PSS that aims to integrate, enable, and support intelligent products and services through the use of ICT. An information technology (IT) driven business strategy that uses intelligent systems as infrastructure, media and tools as intelligent commodities, and electronic services as the principal value given is the foundation of the innovative PSS model. Stakeholders become active actors in this

approach. Meeting the specific needs of each customer is its steadfast commitment. When it comes to the connection between a company's internal capabilities and the diversity of its services, research on stakeholders shows that external alliances are crucial (Iinuma et al., 2022). Determines how various policies have influenced the growth of small and medium-sized businesses. Outline the steps involved in developing and sharing new knowledge inside and between organisations.

Warnakulasooriya, study the elements that affect the demand for products among millennials and Gen Z. Examine the needs of PSSs in light of the variety of consumer demands (Hou et al., 2023). To fulfil the demands of remanufacturing clients, devise service optimisation solutions. Create web-based offerings that cater to customers' habits as they navigate the web. It was shown that smart PSS can cross boundaries, is capable of dynamic capacities, and has consequences for value systems and business models.

2.3 Electromagnetic actuator designs

The inherent advantages of electromagnetic actuation principles are significantly increasing their appeal in MEMS. Numerous microsystem applications are being explored as possible uses for electromagnetic actuators due to their unique properties. Numerous technologies, including those for medical, energy harvesting, microfluidics, microrobotics, and microoptical systems, exist on the microscale (Sharma et al., 2023). The electromagnetic actuation method utilises electric currents and magnetic field interactions to deliver dependable actuator operations, even in the face of severe system constraints, in contrast to electrostatic, piezoelectric, and thermal actuation methods. Electromagnetic actuators used in microelectromechanical systems (MEMS) fall into one of three main categories: those that use Lorentz forces, those that use magnetic attraction or repulsion, and those that use other forms of forces. Each of these types achieves targeted actuator behaviours appropriate for specific microdevice requirements by utilising different electromagnetic interactions (Lv et al., 2024). The basic idea behind Lorentz force actuators is the force that a current-carrying conductor experiences when enclosed in a magnetic field. The actuation responses of Lorentz force actuators are linear, extremely accurate, and predictable because they control electric currents and magnetic fields on a microscale.

Microsystems, including micropositioning stages, optical switching devices, and micro-scanners, rely on these actuators for accurate motion control due to their high repeatability, fast response time, and enormous displacement capabilities (Cheng et al., 2025). Actuators that rely on the attraction or repulsion of magnetic fields can tap into the inherent forces of magnets and soft magnetic materials. These do not depend on dynamic current flow like Lorentz force actuators do; instead, they use changes in magnetic permeability and static or semi-static magnetic fields.

3 Research methodology

The measured component is typically integrated into traditional electromechanical systems using embedded sensing devices with flexible architectures, typically based on sensing coils or magnetic elements. As seen in Figure 1, the integrated position detection system is proposed to start with a basic, generic NC rotary table. There is a worm gear, a

bearing, and a mechanical drive that make up the NC rotary table's motor and gearbox, respectively. Metering equivalency is achieved by means of the embedded time grating and the equal space indexing of the motor, gears, and steel balls. A comparable processing system can locate all electromechanical components using the same excitation signal and clock frequency [Figure 1(b)] because of to the integrated sensing element.

Figure 1 (a) Schematic representation of a permanent-magnet synchronous motor with an integrated time grating sensor and worm gears (b) The optical sensing system's simulation model and experimental validation, displaying features of the radiant output, the imaging effect, the region of light transmission, and the light source (see online version for colours)

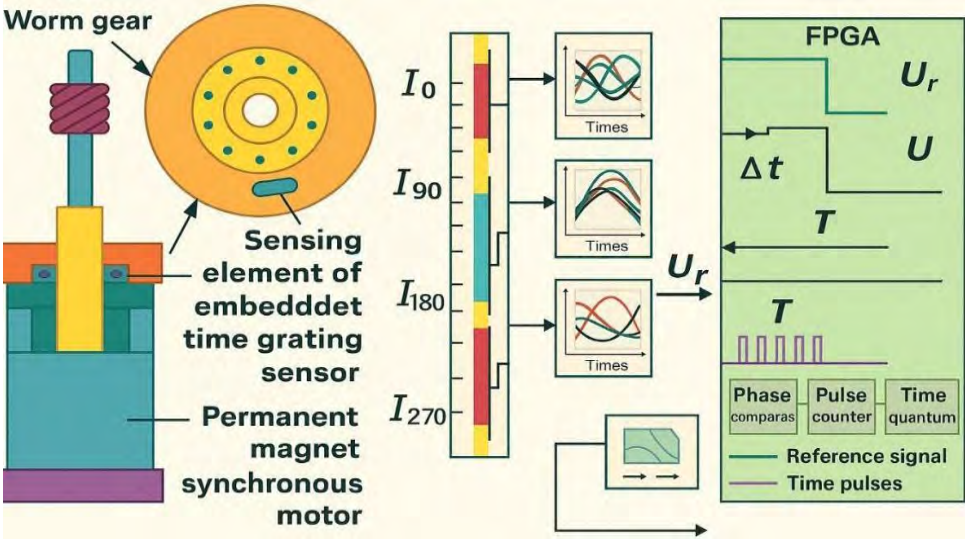

(a) (b)

3.1 A coils embedded sensing head

Most magnetic sensors are coils that use electromagnetic induction to detect magnetic fields. A self-cogging gear-shaped rotating body, an iron core, an induction coil, and an excitation coil make up the coil-based sensing unit. Two separate kinds of formations are shown in Figure 2 (Wang et al., 2024). The motor configuration, as shown in Figure 2(a), is typical of actuators that use self-cogging mechanisms. An induction coil surrounds the teeth, while three-phase excitation coils encircle the electromechanical devices' static components and the rotating body. According to the time grating principle, this can only function with a moving field that is significantly faster than the reference system's velocity. A high-frequency voltage excites the excitation coils, which in turn cause the induction coil to generate a travelling signal. Another differential structure example can be found in Figure 2(b). The self-cogging structure of the measured object spins in tandem with the common core, excitation coils, and induction coils of the sensor. This device achieves spatial orthogonality by controlling the winding process, rather than utilising sensing elements spaced a quarter of the pitch apart. When applied to applications that are short in space, this reduces bulk and provides obvious benefits. The

identical effect can be obtained by positioning two secondary windings that signal SIN or COS at right angles to each other.

Figure 2 The sensing coil allows the embedded time grating sensor to be configured in two ways, (a) using an induction coil on the spinning segment and an excitation coil on the stationary part (b) with both coils wound on the stationary part (see online version for colours)

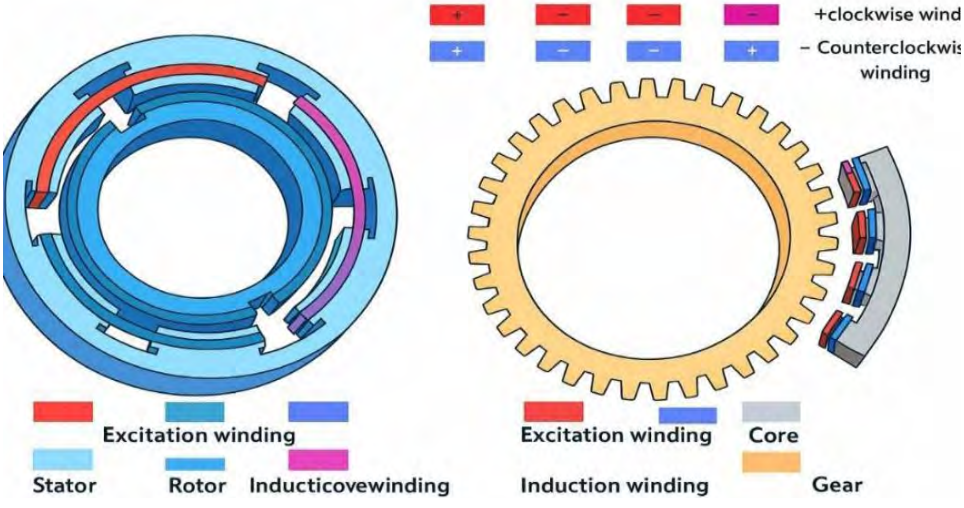

(a) (b)

Unlike the traditional inductive sensor, which measures displacement by monitoring the change in inductance. The air-gap magnetic permeance (AGMP) changes at regular intervals because the core and gear are so far apart. In a perfectly aligned set of teeth, the AGMP is at its lowest, and in an uneven set of teeth, it is at its highest. Here we take into account the basic and constant component, the AGMP, as well as the mathematically defined displacement *x*, which is:

$$A = A_0 = A_m COS\left(2\pi \frac{x}{W}\right) \tag{1}$$

where W stands for the tooth pitch, The constant component is denoted by Λ_0, Λ_m is used to represent the amplitude of the basic component. Equations (2)–(8) define the output voltage of the induction coil with the coil architecture and winding illustrated in Figure 4(b). To turn on the excitation coil, one must alter the current signal.

$$\begin{aligned} E_1 &= -N_2 \frac{d\varnothing}{dt} = -N_2 \frac{d\left(N_1, l_A\right)}{dt} = N_1 N_2 A \frac{d\left(l_m \sin wt\right)}{dt} \\ &= -\left(A_0 + A_m COS\left(2\pi \frac{(X)}{W}\right)\right) COSwt \end{aligned} \tag{2}$$

$$E_2 = -N_2 \frac{d\varnothing}{dt} = -k\left(A_0 + A_m COS\left(2\pi \frac{\left(x + (3/4)W\right)}{W}\right)\right) COS(wt) \tag{3}$$

$$E_1 = -N_2 \frac{d\varphi}{dt} = -N_2 \frac{d\left(N_1 I_\Lambda\right)}{dt} = -N_1 N_2 \Lambda \frac{d\left(I_m \sin wt\right)}{dt} = -k\left(\Lambda_0 + \Lambda_m \cos\left(2\pi \frac{x}{w}\right)\right)\cos wt \tag{4}$$

$$E_2 = -N_2 \frac{d\varphi}{dt} = -k\left(\Lambda_0 + \Lambda_m \cos\left(2\pi \frac{x(3\backslash 4)w}{w}\right)\right)\cos wt \tag{5}$$

$$E_3 = -N_2 \frac{d\varphi}{dt} = -k\left(\Lambda_0 + \Lambda_m \cos\left(2\pi \frac{x(6\backslash 4)w}{w}\right)\right)\cos wt \tag{6}$$

$$E_4 = -N_2 \frac{d\varphi}{dt} = -k\left(\Lambda_0 + \Lambda_m \cos\left(2\pi \frac{x(9\backslash 4)w}{w}\right)\right)\cos wt \tag{7}$$

$$E_s = E_1 + E_2 + E_3 + E_4 = -2\sqrt{2k}\Lambda_m \cos(wt)\sin\left(2\pi \frac{x}{w} + \frac{\pi}{4}\right) \tag{8}$$

where N_1 is the number of turns on the excitation coil and N_2 is the number of turns on the induction coil. This equation includes the following variables: k, dental pitch, amplitude of excitation current, magnetic flux, and angular frequency of current. As an example, let us consider the sensor that uses two group coils. The second group uses a variety of winding algorithms to generate a winding spaced distance d, where m = 0, 1, 2, and W is equal to (m + 1/4). This results in a moving coordinate system. Here, we find d as (9/14) served as an illustration. Except for the fact that the two excitation signals are in phase with one another, they are identical. The induction voltage is also calculated using the formula.

$$E_1' = -N_2 \frac{d\varphi}{dt} = -N_1 N_2 \Lambda \frac{d\left(I_m \sin wt\right)}{dt} = k\left(\Lambda_0 + \Lambda_m cps\left(2\pi \frac{x}{w}\right)\right)\sin wt \tag{9}$$

$$E_2' - N_2 \frac{d\varphi}{dt} = -k\left(\Lambda_0 + \Lambda_m \cos\left(2\pi \frac{x + (3\backslash 4)w}{w}\right)\right)\sin wt \tag{10}$$

$$E_3' - N_2 \frac{d\varphi}{dt} = -k\left(\Lambda_0 + \Lambda_m \cos\left(2\pi \frac{x + (6\backslash 4)w}{w}\right)\right)\sin wt \tag{11}$$

$$E_4' - N_2 \frac{d\varphi}{dt} = -k\left(\Lambda_0 + \Lambda_m \cos\left(2\pi \frac{x + (9\backslash 4)w}{w}\right)\right)\sin wt \tag{12}$$

$$E_c = E_1' + E_2' + E_3' + E_4' = -2\sqrt{2k}\Lambda_m \cos(wt)\cos\left(2\pi \frac{x}{w} + \frac{\pi}{4}\right) \tag{13}$$

By connecting the windings in series, we may determine the total output voltage E.

$$E = E_s + E_c = 2\sqrt{2k}\Lambda_m \sin(wt)\cos\left(2\pi \frac{x}{w} + \frac{\pi}{4}\right) \tag{14}$$

To calculate the displacement, which is part of the travelling signal's phase, one can utilise the time grating to count the time pluses.

3.2 Single-resistor based current reconstruction techniques

For three-phase permanent magnet synchronous motors, the most typical circuit layout is a three-phase full-bridge voltage source inverter. The use of two-or three-phase current sensors is common for detecting phase current in this setup, it is feasible to reconstruct three-phase current using just one current sensor by storing data on winding phase current in the current branch (Chen et al., 2022). Based on the states of the inverter's switches, eight space voltage vectors are shown in Figure 3. Assuming a positive input and a negative output from the motor, six of these vectors will have voltages greater than zero and two will have voltages equal to zero. Any two power tubes' branch currents will vary according to the switching states, therefore you may reconstruct the phase current by combining the various permutations of switches. Two sectors' boundaries and one's reconstructable area make up every nonzero voltage vector. The correlation between the currents flowing through each branch and the currents flowing through the windings is displayed in Table 1. According to the data in the table, the current flowing through the inverter's many branches varies as the switching state changes, and each branch stores information about its own unique phase current.

One new approach is to start and end each pulse width modulation (PWM) cycle with zero voltage vectors, respectively. Figure 3 shows that at the beginning and conclusion of every PWM cycle, as well as in the midway, the zero vectors 0 and 7 are injected. Voltage vectors that are effective make up the remaining sections. Finding the third phase current on a PWM cycle is possible with a single current sensor sampling two phase currents under two different voltage vectors at various points on the cycle. An effective vector's working duration must exceed the minimum sampling time for stable current sampling to take place, which necessitates taking into account the sample process, the switch process, and the time needed to convert from analogue to digital. The connection between time factors is as follows:

$$T_{\min} = T_d + T_{set} + T_{con} \tag{15}$$

Table 1 Correlation among DC-link voltage and current

Voltage vector	*Switch states (upper)*	*DC-link current (dc)*
5	001	
4	011	–
3	010	
2	110	–
1	100	
0	000	0

The total amount of time required for a microprocessor sampling module to transition from sampling to digital data conversion, denoted as includes both the deadzone time and the time it takes for the transient process to occur during a state shift of the switch tube. Phase current data cannot be acquired in the non-sampling area, which encompasses the sector boundary region. This non-sampling area's sampling time is minimised via a unique SVPWM modulation method. Based on Figure 3, Figure 4 displays the seven-segment pulse width modulation (PWM) waveform generated by the SVPWM

algorithm. Following this sequence applies the reference voltage vectors for one period: 0→, 1→, 2→, 7→, 2→, 1→, 0→. The waveform is shown to be symmetrical.

Figure 3 Voltage space vector composition, (a) vectors in different regions (b) in the same sector, the reconstructable vector 2 is a vector (see online version for colours)

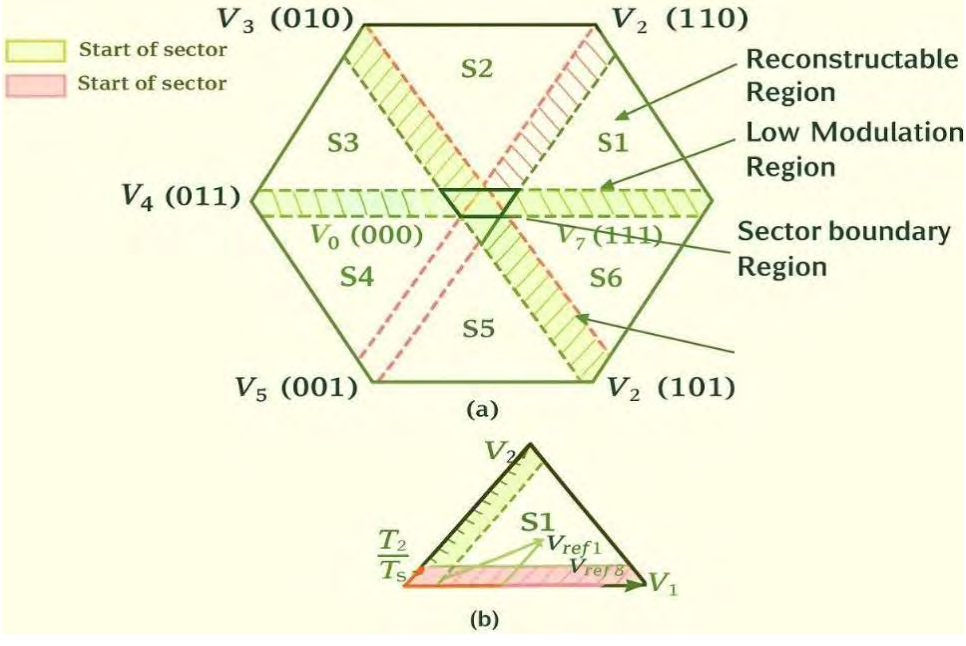

Figure 4 Reference voltage vectors and their effect on output current (see online version for colours)

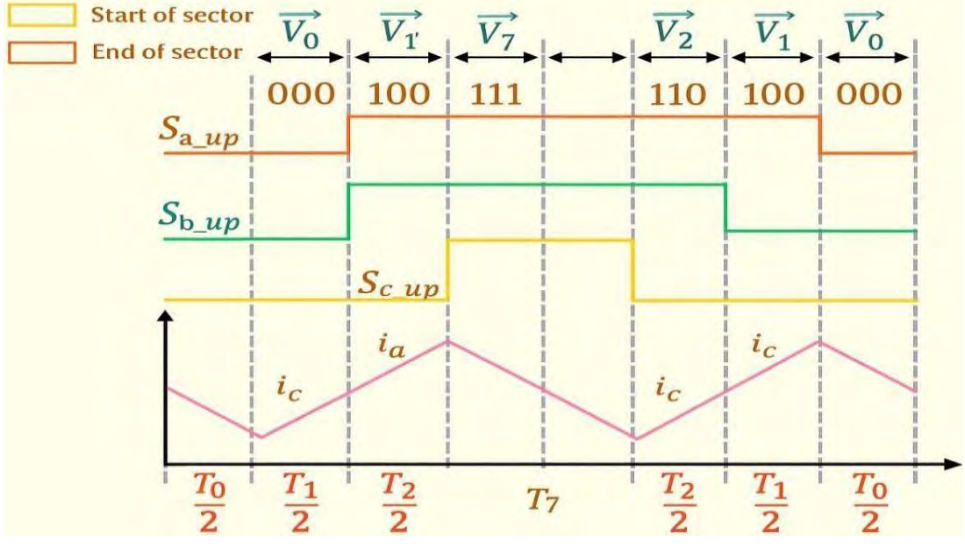

Figure 5 This is the present trajectory of the reference vectors for voltages that are not zero, (a) Sa = 1, Sb = 0, Sc = 0 (b) Sa = 1, Sb = 1, Sc = 0 (c) Sa = 0, Sb = 1, Sc = 0 (d) Sa = 0, Sb = 1, Sc = 1 (e) Sa = 1, Sb = 1, Sc = 0 (f) Sa = 0, Sb = 1, Sc = 0 (see online version for colours)

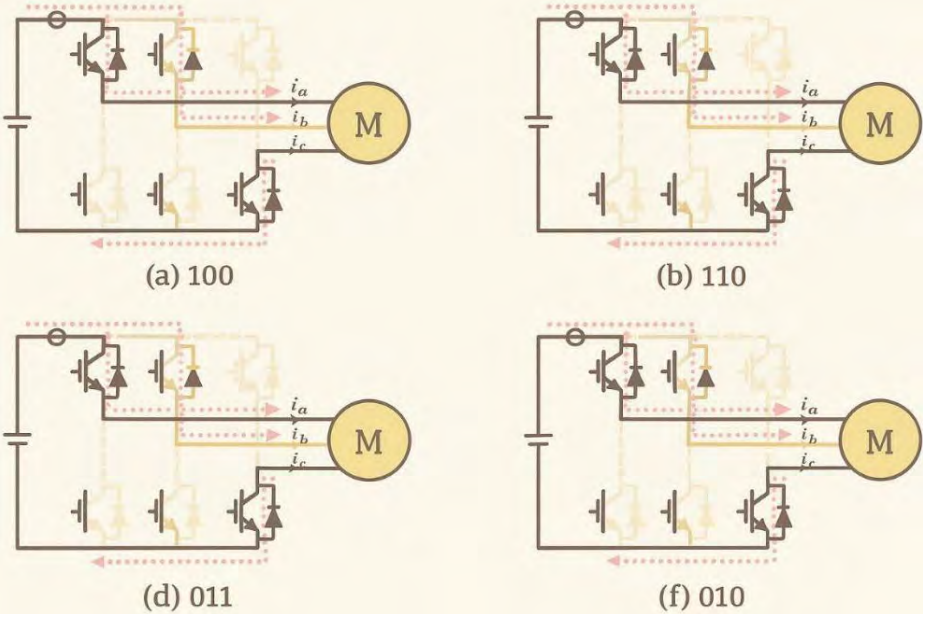

Figures 5 and 6 display the paths of the current as it flows under various vectors. The symbol stands for the three-phase power electrical equipment's switching state. To activate the low switch of the i-phase and deactivate the high switch, the phase-to-current ratio must be zero. In contrast, the low switch and high switch of the i-phase are both activated when = 1.

Figure 6 Two reference vectors' current paths at zero voltage, (a) Sa = 1, Sb = 1, Sc = 1 (b) Sa = 0, Sb = 0, Sc = 0 (see online version for colours)

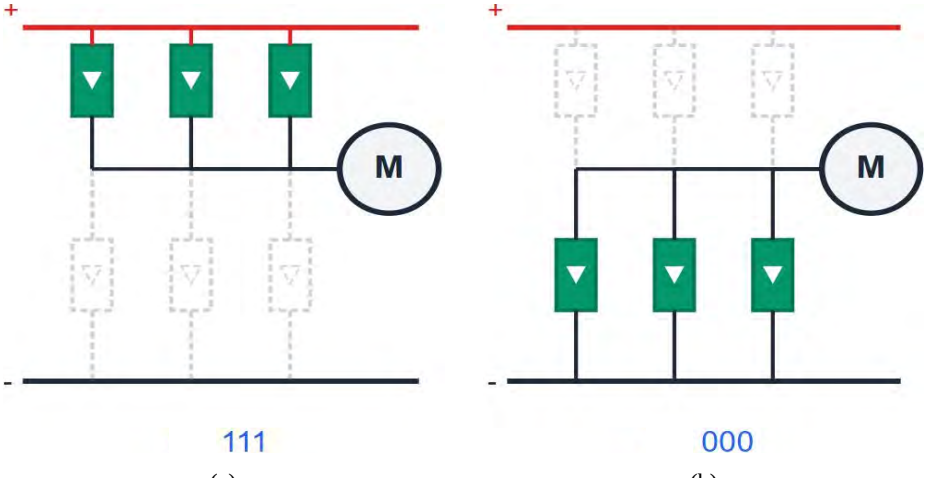

(a) (b)

3.3 Scattering model and error analysis

The optical effect of a collimated LED is the same as that of an extremely long focal length point source. Light scattering model at a particular divergence angle from a collimated LED is shown in Figure 7(a) (Fu et al., 2020). When light is emitted, its width can be altered by the processes of refraction and scattering.

As seen in Figure 7(a), the light transmission area widens or shrinks depending on the incidence angle, with a greater range of values observed for steeper angles. There are clear differences in the light transmission zones on either side of the centreline due to the core symmetry of the point source. The spatial phase shift will become significantly off as a result of this incident. The sides of the centreline that are to the left and right of it exhibit distinct phases. This causes the light transmission zones to have spatial phases that are either ahead of or behind the ideal phase, depending on the incidence angle, at the left and right sides of the centreline. Rearranging the four sets of light transmission surfaces along the centreline results in a reversal of the phase shift values, as illustrated in Figure 7(b). Since the angle of incidence of light varies depending on location, Light transmission surfaces will also exhibit different phase shifts. When the areas of all the surfaces in the set are combined together, though, the light signal remains constant. Taking the mean phase shift of a group of identical light transmission surfaces simplifies the definition of phase offset. The following expression can be used to represent the light transmission area, as shown in Figure 7(b).

$$s(x) = 2\int_0^{x+\Delta x} A\sin(\pi x \setminus w)dx = (2w \setminus \pi)\left\{1-\cos\left[(x+\Delta x) \setminus w\right]\right\} \tag{16}$$

Figure 7 A model for the propagation of light from a luminous source, (a) central symmetric phase deviation model and its application (b) the mean phase difference between light-transmitting surfaces (see online version for colours)

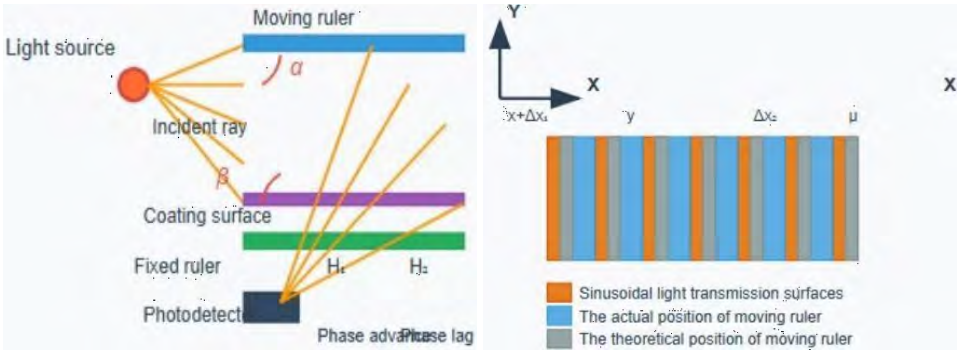

(a) (b)

The actual movement of the ruler in motion is denoted by x. Positioning light transmission surfaces to the right of the centreline (0° and 180°) results in a positive phase shift of Δx, –Δx is the negative phase shift that occurs when they are positioned to the left of the centreline, namely at 90° and 270°. Pictured in Figure 7(b) is this setup.

$$e(x) = \arctan\left(\sin\left[\pi(x-\Delta x \setminus w)\right] \setminus \cos\left[\pi(x-\Delta x)\right]\right\} - \arctan\left[\tan(\pi x \setminus w)\right] \tag{17}$$

Figure 8 The phase shift of Δx causes the variation law, (a) the curve showing the errors (b) elements of the mistake (see online version for colours)

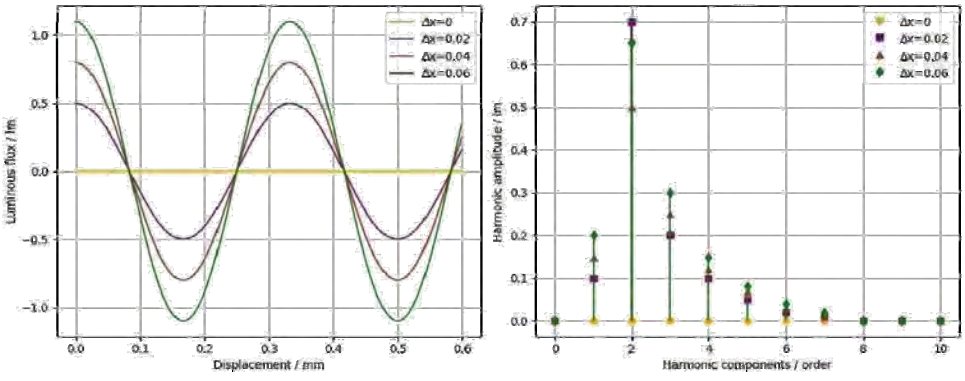

(a) (b)

While it is possible to simulate the phase shift Δx using software, it is challenging to directly analyse the error connection using equation (17) due to the complexity of the inverse trigonometric function. Equation (17)'s error curve, simulated in MATLAB with a 0.6 mm light transmission surface width, is shown in Figure 8(a). There is a clear periodicity to the error variation, which generally indicates a second-order error within a one-period (0.6 mm) range. Additionally, when the phase shift Δx grows, so does the measurement inaccuracy. Figure 8(b) illustrates the outcome of applying Fourier spectral analysis to the error curve; according to the results, dispersion is the most important cause of inaccurate results, whereas second-order harmonic components are the primary culprits in terms of mistake.

4 Results and discussion

To carry out the experiments, the electromechanical self-sensing system prototype is utilised. This test relies on the following critical parameters: At 800 S/s, the motor is collecting data at an excitation frequency of 400 Hz while rotating at 160 rpm. The maximum allowable excitation frequency is, of course, 40 kHz. See to it that the turntable is adjusted to spin at a speed of one revolution per minute. There is a 2.4° gap between the motor, worm gear, and bearing data points, and a 0.015° gap between the two sets of observations. Using embedded time grating sensors, Figure 9(a) shows the position curves of the bearing and worm gear in 60 s, while Figure 9(b) shows the motor's in 0.75 s. The worm gear and bearing produce nearly identical detection data as a result of their synchronised rotation, as illustrated in the pictures. Even though the motor is spinning faster, it has completed two full revolutions in 0.75 seconds.

It is during detection that discrepancies between the observed and theoretical data are identified. There were a lot of mechanical processing, installation, and electrical error-related system errors in it. Figure 10 shows that after correcting the error according to its amplitude-frequency characteristics, a considerable number of random errors persist. Accuracy levels of 0.06° for the bearing, 0.024° for the worm gear, and 0.20° for the motor are all within the range of practical use. The motor has a maximum range of

0.06°, 0.024°, and 0.20°. The driver, gearbox, and motion components' detecting accuracy is clearly different from one another.

Figure 9 Location details, (a) worm gear with bearing (b) servo motor (see online version for colours)

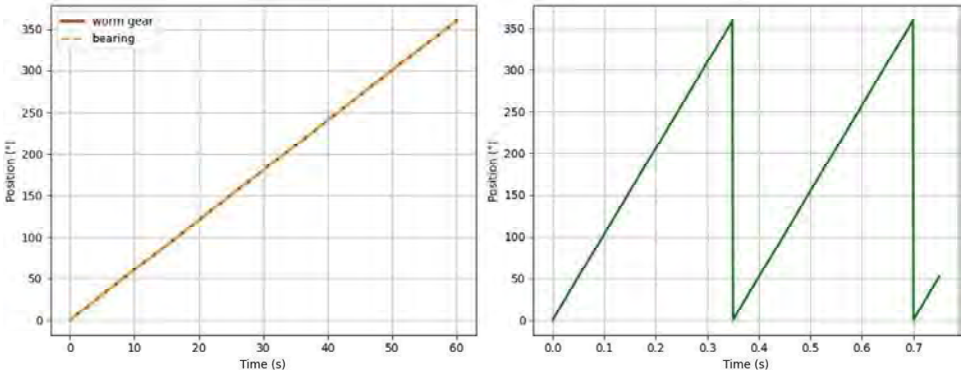

(a) (b)

Figure 10 Data on detection errors acquired after correction (see online version for colours)

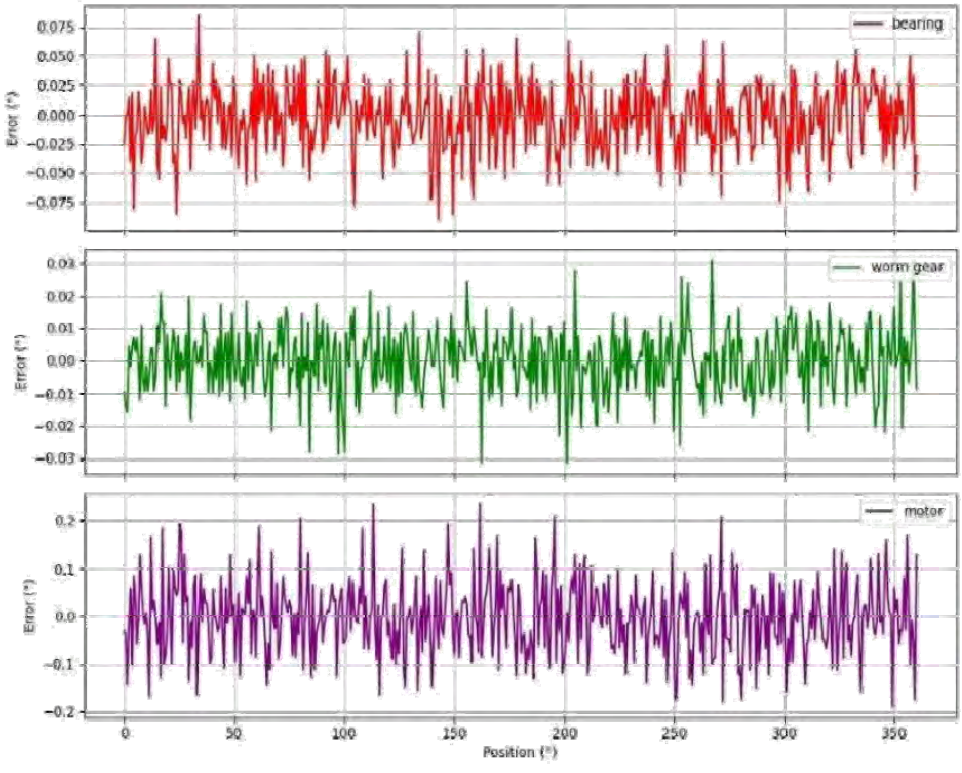

Following the standard practice of closed-loop control in electromechanical systems, we feed the command bearing feedback and the motor's fusion error data. According to the adaptive weighted averaging method that was previously mentioned, the relevant parameters may be found in Table 2. After fusing, the resultant error curve is shown in Figure 11. After merging, the data can deviate by more than ±0.012°. The control precision is increased by nearly eight times when compared to semi-closed-loop control, which simply relays the servo motor's measurement error to the command.

Figure 11 Integrated data of motor and bearing fault detection errors (see online version for colours)

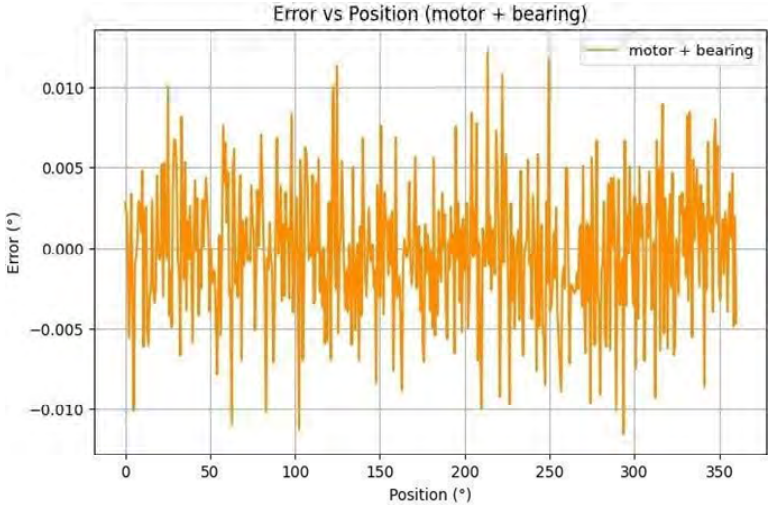

A shared processing system detects the positions of all electromechanical system components and uses adaptive weighted averaging to optimise them. The detection data for bearing and worm gear are fused first because of their comparatively better precision synchronous motion display. These findings are transformed for use at high speeds and combined with the motor's detection error data in accordance with the gearbox ratio. Table 3 displays the important parameters, and Figure 12 shows the curved final error data. The three-error data fusion yields an error value of 0.004° within the 360° range of measurable values; the combined motor and bearing detection is almost six times more effective, and the individual motor detection as feedback is around 48 times more effective. Based on these comparisons, it is clear that combining the measurement errors of the individual components significantly lowers the overall error. When the post-fusion error and the instruction are used as the actual positioning value, positioning detection becomes significantly more precise.

Table 2 The bearing's and motor's relative fusion data parameter

Component	*Mean value*	*Std. deviation*	*Fusion factor*
Bearing	-5.75×10^{-4}	0.0386	0.9843
Motor	0.0354	0.0049	–

Figure 12 Mixture of gearbox, bearing, and motor faults (see online version for colours)

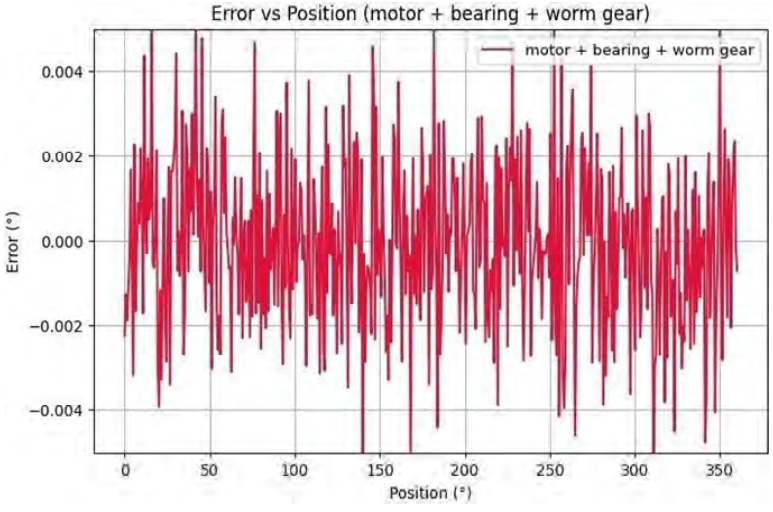

Table 3 Bearing, worm gear, and motor error fusion parameter comparisons

Parameter	*Bearing*	*Worm gear*	*Motor*
Mean value	-5.75×10^{-4}	–0.0027	–
Standard deviation	0.0049	–0.0103	
Fusion factor	0.182		
Mean of fused data	-9.522×10^{-4}	0.0354	
Std. deviation of fused data	0.0041	–0.0386	
Fusion factor (fused data)	0.989		

Figure 13 Ratio of adaptive to traditional RBFNN two-phase stator current waveform, (a) three-phase current waveform of RBFNN (b) three-phase current waveform of adaptive RBFNN (see online version for colours)

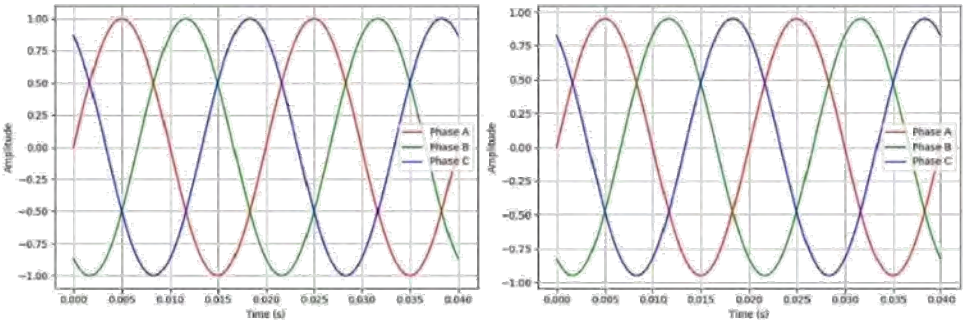

(a) (b)

It is possible to construct the experimental platform using the hardware system design, the SPMSM mathematical model, and the sensorless control approach. This platform relies on an ac servo motor, power supply, drive circuit, and oscilloscope. Before turning

on the ac servo motor, the TMS320F28335 – the control system's central processing unit. By regulating the inverter's switching tube in the driving circuit, this driving signal can restore normal operation to the servo motor. To avoid damaging the motor, powering it up is contingent upon the output driving signal meeting certain standards. The experiment with the ac servo motor's sensorless control is conducted once the main control chip's ability to generate the control signal has been verified. Once the rotation speed hit 1,000 rpm, the experiment could begin if the position-free control system could function in sliding mode. Table 4 displays the precise specifications of the servo motor used in the experiment. The three-phase waveform of the stator current is shown in Figure 13.

Table 4 Key parameters of the AC servo motor

Parameter	*Value*
Voltage of nominal	48 V
Speed of nominal	1,000 RPM
Pout	1 kW
T_Rated	3.18 N•m
Rs	0.2 Ω
P	6
Specification	Value

Figure 14 Waveform recognised via an interface between humans and machines, (a) stator current waveforms in three phases (b) current waveforms after Clarke transformation (c) signals from SVPWM (d) curves comparing actual and reference speeds (e) plots showing real versus estimated rotor positions (f) response dynamics when reference speeds are varied (see online version for colours)

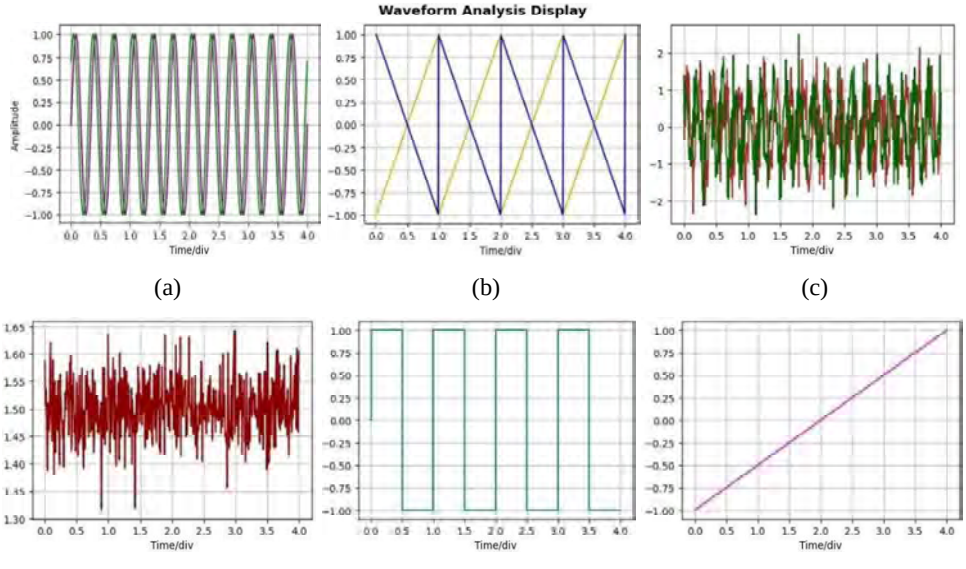

Figure 13 shows the three-phase current waveform both before and after RBFNN utilised the adaptive technique. It is evident that the harmonic wave is eliminated under the

identical circumstances. Figure 14 illustrates the waveform captured by the higher-level software; Figure 14(d) demonstrates that the suggested approach accurately tracks the reference value; Figure 14(e) demonstrates that the rotor position can be anticipated with high precision; and Figure 14(f) demonstrates that a rapidly increasing rotor speed is possible without overrun.

The innovative fixed ruler depicted in Figure 15(a) was created and built using symmetrical structures and continuous cosinusoidal light transmission surfaces. Measurements were more accurately captured when this ruler was used in conjunction with the previous research to mitigate the effect of the light-field distribution. Figure 15(a) shows that there were eight sets of identical light-transmitting surfaces. To guarantee that the stationary and movable rulers were set up in tandem, the other four surfaces served as installation flags. To record the signals of light transmission, the 12-photocell integrated photodetector was set up as shown in Figure 15(b). We designated four channels for installation signals and eight for modulated light intensity signals.

In Figure 16, we can observe the outcomes of a comparison experiment that was conducted using this optimised fixed ruler in conjunction with two light sources that were previously used on the identical experimental platform. Figure 16 showed the curves representing the measurement errors.

Figure 15 Schematic of the positioning module showing photocell orientations and alignment with the positioning part (see online version for colours)

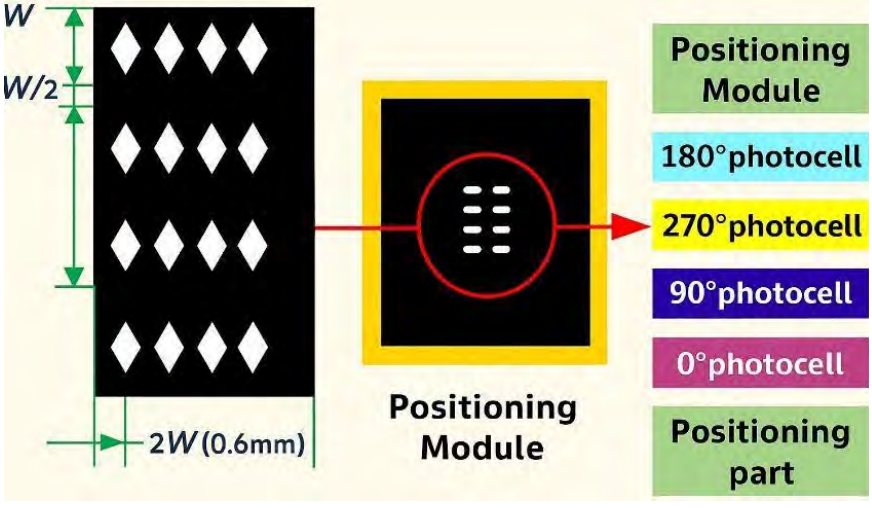

First-, second-, and third-order harmonic errors are the most significant factors influencing measurement error, as seen in Figures 16 and 17. By getting rid of fourth-order harmonic errors, we were able to drastically cut down on the overall mistake. The measurement inaccuracy decreased from 0.79 to 0.4 μm in the 0.6 mm range when the light scattering angle was 1.8°. At a scattering angle of 5.5°, the measurement error dropped from 1.07 to 0.5 μm. As shown in Figures 16(a) and 16(b), the second-order harmonic error remained essentially unchanged, even though the measurement error rose by 0.1 μm. Earlier studies have shown that second- and fourth-order harmonic measurement errors are mostly caused by the scattering angle.

Experimental results demonstrate that the enhanced fixed ruler successfully mitigates light source scattering error. Theoretical and simulation investigations corroborate the findings of the comparative trials, which reveal that the new design significantly enhances measurement accuracy. The movable ruler was then advanced by 1 mm increments using the linear motor, collecting 500 position data points over a 500 mm distance. Figure 17 shows the measurement inaccuracy as a blue error curve. With a peak-to-peak measurement of 2.4 μm, the error has a width of approximately 0.4 μm.

Figure 16 Harmonic error components and measurement error curves for symmetrical constant cosine light transmission floors, (a) 1/2 = 5.5° (b) 1/2 = 1.8° (see online version for colours)

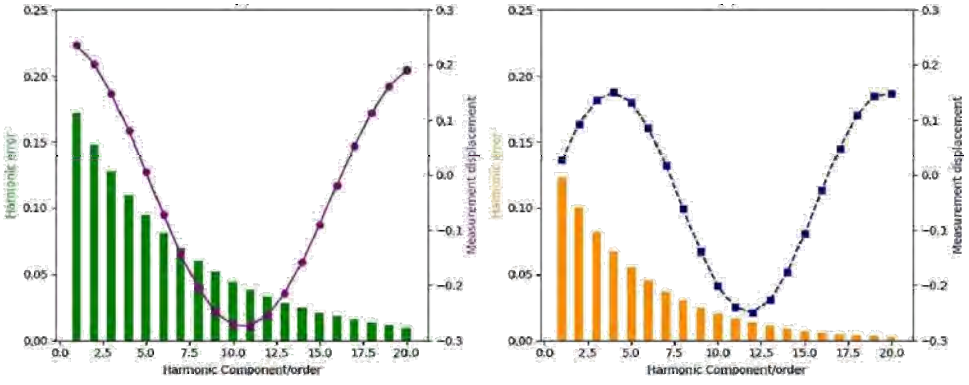

(a) (b)

Figure 17 Accuracy of measurements for optimising structures over extended periods of time (see online version for colours)

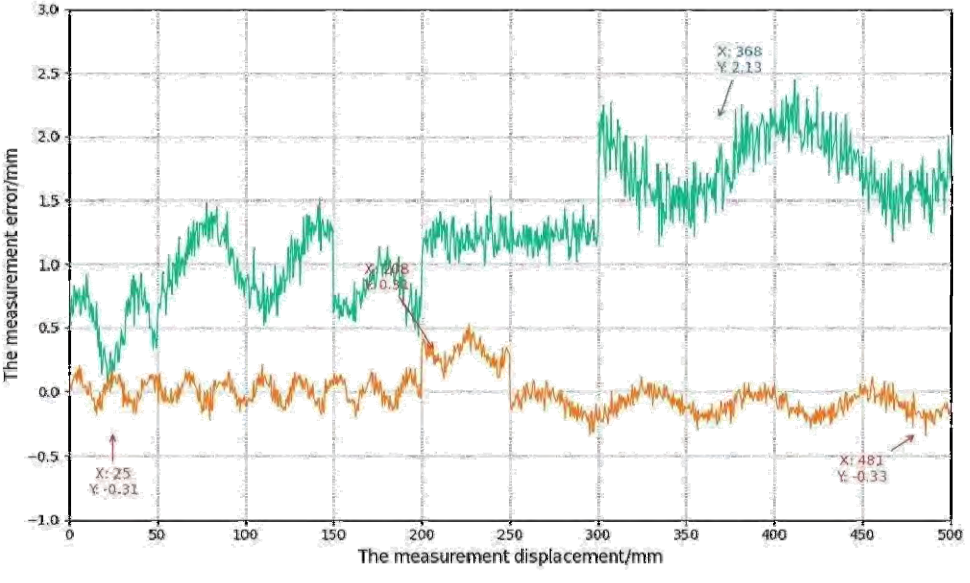

Notes: The blue line indicates the amount of uncorrected error, while the red line indicates the amount of corrected error.

An error during installation or manufacturing might cause a low-frequency error to extend across the entire range, which in turn causes the principal error components. Regular adjustments to the sensor mounting structure and calibration of the observed value with the laser interferometer measurement are necessary to eliminate low-frequency inaccuracies. This is due to the fact that the long-period error displays a consistent pattern of variation throughout the whole range. The red error curve in Figure 17 demonstrates that, after accounting for errors, the ultimate measurement precision over a 500 mm range is 0.64 μm.

5 Conclusions

This research demonstrates that electromechanical systems can greatly enhance their position detection accuracy and decrease their system faults by incorporating time-grating displacement sensors. Measurement precision down to 0.64 μm was accomplished by the proposed methodology through the development of sensing heads, optimisation of optical structures, and current reconstruction approaches. When compared to single-sensor detection, the experimental results show that positioning errors are nearly 48 times reduced when motor, worm gear, and bearing data are fused. System stability is further ensured by the use of adaptive algorithms for motor control, which improve real-time tracking and reduce harmonic distortions. The results show that smart product applications may be built on a solid basis of intelligent monitoring and control thanks to the integration of embedded sensors, electromechanical design, and modern signal processing.

Declarations

All authors declare that they have no conflicts of interest.

References

Abouzeid, A.F. (2022) 'Co-simulation-based verification of torsional vibration protection of electric-driven railway vehicle wheelsets', *Vibration*, Vol. 5, No. 3, pp.613–627.

Akbar, S., Vaimann, T. and Asad, B. (2023) 'State-of-the-art techniques for fault diagnosis in electrical machines: advancements and future directions', *Energies*, Vol. 16, No. 17, p.6345.

Arioli, V., Ruggeri, G. and Sala, R. (2023) 'A methodology for the design and engineering of smart product service systems: an application in the manufacturing sector', *Sustainability*, Vol. 15, No. 1, p.64.

Chen, H. and Cai, C. (2022) 'High-speed control of AC servo motor using high-performance RBF neural network terminal sliding mode observer and single current reconstructed technique', *Electronics*, Vol. 11, No. 10, p.1646.

Chen, Y. and Visnjic, I. (2021) 'On the road to digital servitization – the (dis)continuous interplay between business model and digital technology', *Int. J. Oper. Prod. Manag.*, Vol. 41, No. 5, pp.694–722.

Cheng, J. and Xue, N. (2025) 'Recent design and application advances in micro-electro-mechanical system (MEMS) electromagnetic actuators', *Micromachines*, Vol. 16, No. 6, p.670.

Cirstea, M. and Benkrid, K. (2024) 'Digital electronic system-on-chip design: Methodologies, tools, evolution, and trends', *Micromachines*, Vol. 15, No. 2, p.247.

Fakhraian, E. (2023) 'Towards safe and efficient unmanned aircraft system operations: literature review of digital twins' applications and European Union regulatory compliance', *Drones*, Vol. 7, No. 7, p.478.

Fu, M., Li, C. and Zhu, G. (2020) 'A high precision time grating displacement sensor based on temporal and spatial modulation of light-field', *Sensors*, Vol. 20, p.921, DOI: 10.3390/s20030921.

Gasiyarov, V.R. (2023) 'Method for defining parameters of electromechanical system model as part of digital twin of rolling mill', *J. Manuf. Mater. Process.*, Vol. 7, No. 5, p.183.

Helmns, D. and Blum, D.H. (2021) 'Development and validation of a latent thermal energy storage model using Modelica', *Energies*, Vol. 14, No. 1, p.194.

Hou, L., Su, J. and Ye, Y. (2023) 'Exploring the influence of smart product service systems on enterprise competitive advantage from the perspective of value creation', *Sustainability*, Vol. 15, No. 18, p.13828.

Iinuma, M. and Shiba, N. (2022) 'Modelling and simulation of organisational knowledge creation process with consideration of dialogue', *Asian J. Manag. Sci. Appl.*, Vol. 7, No. 1, pp.1–22.

Jalil, M. (2022) 'Evaluating the mediating relationship of social inclusion between digital financial inclusion services, and MSE development in Malaysia', *Asian J. Manag. Sci. Appl.*, Vol. 7, No. 2, pp.103–122.

Langley, D.J. (2022) 'Digital product-service systems: the role of data in the transition to servitization business models', *Sustainability*, Vol. 14, No. 3, p.1303.

Lv, S., Feng, H. and Lou, W. (2024) 'Design and process of force-electric fusion for electromagnetic driven Si based MEMS S&A', *J. Phys. Conf. Ser.*, Vol. 2740.

Sharma, S. and Nabavi, S. (2023) 'Hybrid MEMS actuator with 3 degrees-of-freedom for efficient planar optical switching', *J. Microelectromech. Syst.*, Vol. 32, No. 6, pp.593–603.

Spiliotis, K. and Gonçalves, J.E. (2020) 'Electrical system architectures for building-integrated photovoltaics: a comparative analysis using a modelling framework in Modelica', *Appl. Energy*, Vol. 261, No. 1, p.114247.

Terron-Santiago, C. (2021) 'A review of techniques used for induction machine fault modelling', *Sensors*, Vol. 21, No. 14, p.4855.

Wang, S. and Liu, S. (2024) 'Self-sensing electromechanical system integrated with the embedded displacement sensor', *Sensors*, Vol. 24, No. 13, p.4102.

Yea, M. and Han, K.J. (2020) 'Modified slot opening for reducing shaft-to-frame voltage of AC motors', *Energies*, Vol. 13, No. 3, p.760.